

# Effects of Resonant Magnetic Perturbations on Radial Electric Fields in DIII-D Tokamak

J. Y. Fu<sup>1</sup>, P. F. Liu<sup>2</sup>, X. S. Wei<sup>2</sup>, Z. Lin<sup>2</sup>, N. Ferraro<sup>3</sup>, and R. Nazikian<sup>3</sup>

<sup>1</sup>*Fusion Simulation Center, Peking University, Beijing 100871, China*

<sup>2</sup>*Department of Physics and Astronomy, University of California, Irvine, CA 92697, USA*

<sup>3</sup>*Princeton Plasma Physics Laboratory, Princeton, NJ 08543, USA*

## Abstract

Gyrokinetic simulations of DIII-D tokamak equilibrium find that resonant magnetic perturbation (RMP) drive a neoclassical non-ambipolar electron particle flux, which causes a rapid change of equilibrium radial electric fields consistent with experimental observations during the suppression of the edge localized mode (ELM). The simulation results provide a support for the conjecture that RMP-induced changes of radial electric fields lead to the enhanced turbulent transport at the pedestal top during the ELM suppression. Furthermore, gyrokinetic simulations of collisionless damping of zonal flows show that resonant responses to the RMP decrease the residual level of the zonal flows and damp the geodesic acoustic mode (GAM).

## 1. Introduction

In tokamak high-confinement regime (H-mode) with an edge transport barrier, edge localized modes (ELM) [1] are often observed to drive a large energy flux from the pedestal region to plasma-facing components [2]. The resonant magnetic perturbations (RMP), produced by a set of external coils, have been showed to be effective for ELM suppression/mitigation [3-8]. The mode stability analysis [3, 4] shows that the RMP can stabilize the ELM by enhancing the radial particle transport at the pedestal top, thus preventing the pedestal from reaching the stability boundary. However, the mechanism for the enhanced particle transport at the pedestal top, i.e., density pump-out is not well understood [5, 9]. Meanwhile, a rapid damping of toroidal flows at the pedestal top [10] is often observed during the transition from ELMing to ELM suppression state. This flow damping plays an important role in the turbulent transport that causes the density pump-out at the pedestal top in a

DIII-D shot [11]. The flow damping is mostly caused by a rapid change of equilibrium radial electric fields since plasma pressure profiles change much more slowly during the transition to the ELM suppression. An outstanding issue is that how the 3D RMP causes the rapid change of the equilibrium radial electric fields.

The short timescale of the rapid flow damping implies that the magnetohydrodynamic (MHD) braking effect [12] does not make the dominant contribution. Beyond the MHD theory, several kinetic theories have been proposed to explain the toroidal torque induced by the 3D RMP. In particular, neoclassical toroidal viscosity (NTV) theory [13] suggests that the 3D RMP can induce a radial transport of trapped particles, which generates a toroidal braking torque. Qualitative agreement has been obtained [14-18] between the NTV theory and the braking torque measured in the experiments, but a quantitative discrepancy persists. More importantly, prediction of the particle pump-out associated with the enhanced particle fluxes requires self-consistent calculation of the ambipolar electric fields, which have not been considered in the NTV theory [19].

Recently, gyrokinetic simulations have made impressive progress studying neoclassical and turbulence transport in tokamak with 3D RMP. Gyrokinetic RMP simulations initially used vacuum magnetic field generated by the I-coil without plasma responses [20-23]. A gyrokinetic quasilinear theory [24] predicts an enhanced transport in the pedestal region due to the reduction of the RMP shielding by the reversal of the equilibrium radial electric field on a resonant surface. However, the plasma responses greatly affect the RMP penetration and magnetic island formation [25], which need to be taken into account in the gyrokinetic simulations of neoclassical and turbulent transport. Indeed, gyrokinetic GTC [26] simulations of a DIII-D tokamak equilibrium with plasma non-resonant responses to the RMP find that the 3D equilibrium with closed flux-surfaces does not enhance turbulence transport since the RMP amplitude is too small to have significant effects on linear drift-wave instability or zonal flow damping [27]. Further GTC simulations find that the reduction of the radial electric field shear at the top of the pedestal during ELM suppression leads to enhanced drift-wave turbulence and extended turbulence spreading to the top of the pedestal relative to ELMing plasmas with similar RMP and pedestal parameters [11]. Subsequently, gyrokinetic XGC simulations of the DIII-D equilibrium with both resonant and non-resonant responses to the RMP show that non-ambipolar neoclassical transport can cause a rapid change of

radial electric fields near the magnetic separatrix [28] and that the enhanced turbulent transport can lead to the density pump-out [29].

In this work, we use GTC simulations to study the RMP effects on the radial electric fields including both equilibrium electric fields associated with toroidal rotations and zonal flows generated by microturbulence, which greatly affect the turbulent transport in tokamaks. GTC simulations of the microturbulence and neoclassical transport in 3D toroidal geometry including stellarators [30, 31] and tokamaks with 3D magnetic fields [11, 27, 32-35] have been extensively verified. GTC simulations reported in this paper use realistic DIII-D tokamak equilibrium with both resonant and non-resonant responses to the 3D RMP calculated by the resistive MHD code M3D-C1 [36]. Neoclassical simulation results show that RMP-induced magnetic islands and stochastic electron orbits drive a non-ambipolar electron particle flux, which leads to a rapid change of equilibrium radial electric fields consistent with experimental observations during the transition from the ELMing to ELM suppression state. The GTC neoclassical simulation results on the pedestal top are in qualitative agreement with the XGC neoclassical simulation results near the magnetic separatrix [28] and provide a support for the conjecture that RMP-induced changes of radial electric fields lead to enhanced turbulent transport at the pedestal top during the ELM suppression [11, 29]. Furthermore, GTC simulations of collisionless damping of zonal flows find that resonant responses to the RMP decrease the residual level and damp the geodesic acoustic mode (GAM).

The rest of the paper is organized as follows. GTC neoclassical simulation model for the tokamak equilibrium with the 3D RMP is formulated in section 2. Simulations of neoclassical transport with the RMP without and with equilibrium electric field are presented in section 3 and 4, respectively. In section 5, we calculate the time rate of change of the equilibrium radial electric field due to the non-ambipolar electron particle fluxes. Effects of the 3D RMP on the collisionless damping of zonal flows are discussed in section 6. Finally, conclusions and discussions are discussed in section 7.

## **2. Formulation of neoclassical simulation in tokamak with 3D RMP**

### **2.1 Implementation of tokamak equilibrium with 3D RMP in GTC**

In this work, GTC simulations use magnetic equilibrium with full plasma response to RMP,

including both non-resonant response (which preserves closed flux surfaces) and resonant response (which creates magnetic islands and/or magnetic stochasticity) calculated by the resistive MHD code M3D-C1 [36]. The equilibrium profiles [10, 11, 27] from the DIII-D discharge #158103 at 3050ms, when ELM is suppressed by the n=2 RMP, is chosen as the base case for GTC simulations.

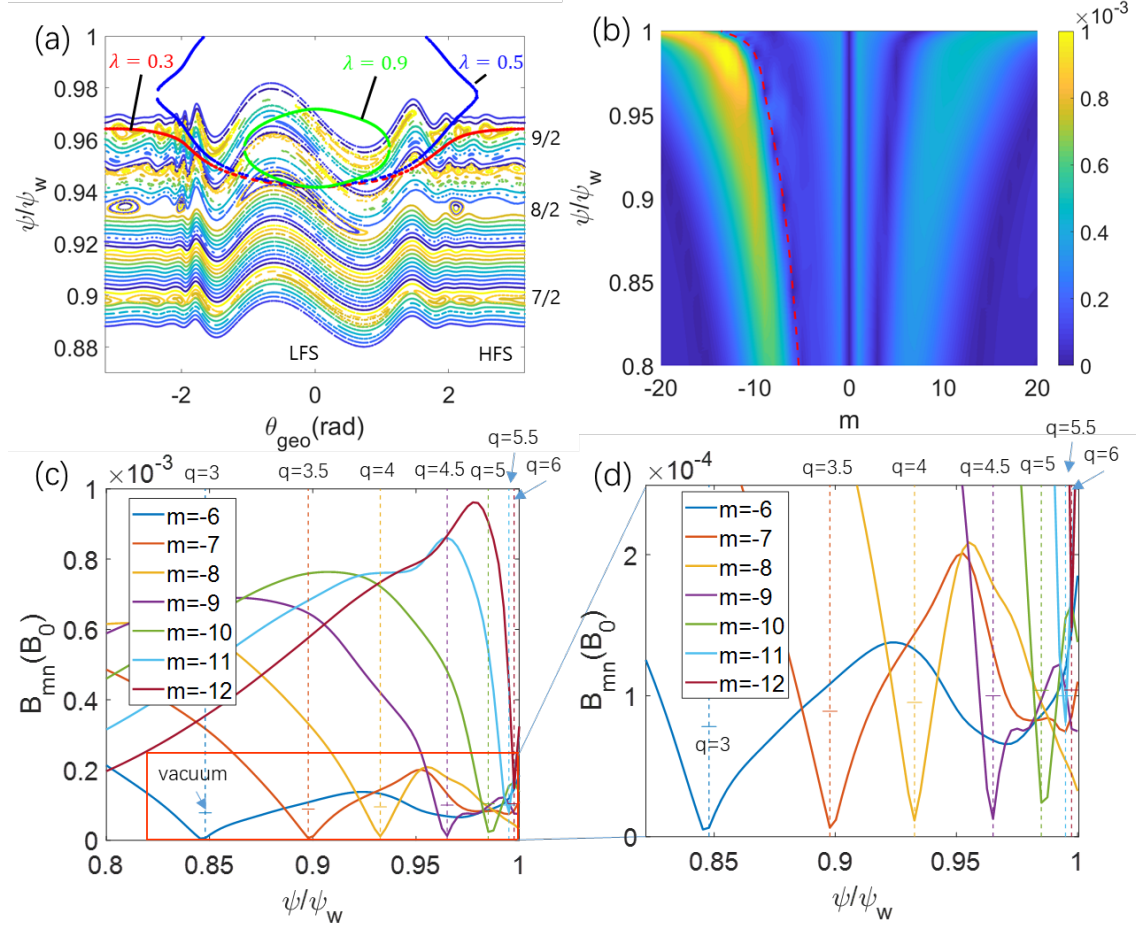


Fig 1. (a) Poincaré plots on the  $\zeta = 0$  poloidal plane for magnetic field lines (small points), and deuterium gyrocenter orbits (red, blue and green big points) for three different pinch angles  $\lambda$  with local thermal speed. Here,  $\theta_{geo}$  (rad) is geometric poloidal angle. (b) Spectrum of n=2 RMP magnetic field as a function of poloidal harmonic  $m$  and poloidal flux  $\psi$ . Dashed red line represents resonant response. (c) Radial profiles of perturbed magnetic fields  $B_{mn}$ , where the red rectangular box is enlarged in panel (d).

The equilibrium magnetic field can be written as  $\mathbf{B} = \mathbf{B}_0 + \delta\mathbf{B}$ , where  $\mathbf{B}_0$  represents the equilibrium magnetic field of an axisymmetric tokamak and  $\delta\mathbf{B}$  represents the 3D RMP. In GTC, the Boozer coordinate  $(\psi, \theta, \zeta)$  is used, corresponding to poloidal magnetic flux, poloidal and toroidal angles. The equilibrium magnetic field can then be represented in covariant form and contravariant form:  $\mathbf{B}_0 = \delta\nabla\psi + g\nabla\zeta + I\nabla\theta = q\nabla\psi \times \nabla\theta + \nabla\zeta \times \nabla\psi$ . Here,  $q$  is the safety

factor,  $2\pi g$  and  $2\pi I$  are poloidal and toroidal currents, and  $\delta$  represents the components of the currents that depend on the poloidal angle. The perturbed magnetic field is cast in GTC using a reduced form  $\delta\mathbf{B} = \nabla \times (\alpha\mathbf{B}_0)$ , which preserves the radial component of perturbed field. The M3D-C1 provides the Fourier series  $\alpha = \sum_{m,n} \alpha_{mn} e^{in\zeta - im\theta}$ , where  $\alpha_{mn}$  is the coefficient of the Fourier series. The function  $\alpha$  calculated by this Fourier series is then converted to a 3D spline function in GTC [27] [37].

Fig. 1(a) shows the Poincare plot of the equilibrium magnetic field with the 3D RMP at the  $\zeta = 0$  poloidal plane, where  $\psi$  is normalized with its value  $\psi_w$  at the last closed flux surface. In the region between  $\psi = 0.87 \sim 0.97\psi_w$ , three island chains  $(m/n) = (-7/2), (-8/2), (-9/2)$  are clearly separated by Kolmogorov-Arnold-Moser (KAM) surfaces. While there is very little stochasticity of the magnetic field lines, the particle orbits may still possess some stochasticity due to the cross-field guiding center drifts that sample multiple magnetic islands. The island widths in the high field side are, respectively, 0.5, 1.5 and 1 in the unit of local proton Larmor radius. Since the 8/2 island is the largest, we focus on the physics around the  $q = 4$  rational flux surface ( $\psi = 0.93\psi_w$ ).

Fig. 1(a) also shows the Poincare plot for deuterium gyrocenter orbits around the  $\psi = 0.95\psi_w$  flux surface with three different pinch angles  $\lambda \equiv \frac{\mu B}{E} = 0.26, 0.5$  and  $0.92$ , which correspond to the typical passing particle, barely trapped particle, and deeply trapped particle, respectively. The guiding center orbits in the region outside of  $\psi = 0.95\psi_w$  could be strongly affected by the magnetic separatrix of the divertor, which is then expected to play the dominant role in the ion neoclassical transport in the pedestal [28]. Since the ion guiding center orbits widths are much larger than the RMP island width around the  $q = 4$  rational flux surface, the RMP islands should not affect the ion neoclassical transport significantly [38], especially when comparing with the dominant role of the magnetic separatrix. Therefore, we neglect the effect of RMP on the ion dynamics, and only study the single-species neoclassical transport of the electron in this work.

Fig. 1(b) shows the poloidal spectrum of the perturbed magnetic field  $B_{mn} = \frac{1}{A} \iint d\zeta d\theta J (\delta\mathbf{B} \cdot \nabla\psi) e^{im\theta - n\zeta}$ , where  $A$  is the surface area of the magnetic flux surface and  $J$  is the Jacobi of the coordinates. The plasma response could be separated into the resonant response and non-resonant response. The resonant response could be quantified by the magnitude of the

perturbed magnetic field at rational surfaces, represented by the red dashed line where  $q = m/n$ . The negative  $m$  of resonant responses indicates the left-handed helicity of the plasma currents.

Fig 1(c) shows the radial profiles of several poloidal harmonics of the RMP. The vertical dashed lines correspond to the radial positions of different rational surfaces. The horizontal short lines correspond to the vacuum RMP field values at the rational surfaces. Fig. 1(d) shows the enlarged red rectangular region in fig. 1(c), where the ratio between the resonant response and the vacuum RMP field value at the  $q = 4$  rational surface is about 0.1, which indicates that the resonant magnetic perturbation is strongly screened by the plasma response.

## 2.2. GTC simulation model of neoclassical transport with RMP and radial electric field

In the GTC neoclassical simulations, the dynamics of electron gyrocenter are calculated by the Hamiltonian [39] in the phase space  $(\mathbf{X}, E, \mu)$ ,

$$H = E - e\phi = \frac{1}{2}m_e v_{\parallel}^2 + \mu B - e\phi,$$

where  $\mathbf{X}$  is the spatial coordinates,  $E$  is the particle kinetic energy,  $\mu$  is the magnetic moment.  $m_e$  is the mass of electron,  $-e$  is the charge of electron,  $v_{\parallel}$  is the parallel velocity along the field line,  $B$  is the amplitude of magnetic field, and  $\phi$  is the electrostatic potential.

The drift kinetic equation describing the guiding center equations of motion based on this Hamiltonian with static magnetic perturbations takes the form

$$L(f_e) \equiv \frac{\partial f_e}{\partial t} + \left( v_{\parallel} \mathbf{b}_0 + \mathbf{v}_d + \mathbf{v}_E + v_{\parallel} \frac{\delta \mathbf{B}}{B_0} \right) \cdot \left[ \left( \frac{\partial f_e}{\partial \mathbf{X}} \right)_{E, \mu} + e \nabla \phi \left( \frac{\partial f_e}{\partial E} \right)_{\mathbf{X}, \mu} \right] - C(f_e) = 0, \quad (1)$$

where  $f_e$  is the electron gyrocenter distribution function,  $\mathbf{b}_0 = \frac{\mathbf{B}_0}{B_0}$ ,  $C$  denotes the Fokker-Plank collision operators, which include inter-species and like-species collisions that conserve particle number, momentum and energy [40]. The drift velocity  $\mathbf{v}_d$  denotes the magnetic curvature and gradient drifts, and  $\mathbf{v}_E$  denotes the  $\mathbf{E} \times \mathbf{B}$  drift. In the absence of magnetic perturbations  $\delta \mathbf{B}$ , the drift velocity could be written as:  $\mathbf{v}_d = -\frac{cm_e v_{\parallel}^2 \nabla \times \mathbf{b}_0}{e B_0^*} - \frac{c \mu \mathbf{b}_0 \times \nabla B_0}{e B_0^*}$ , and  $\mathbf{v}_E = \frac{c \mathbf{b}_0 \times \nabla \phi}{B_0^*}$ . Here,  $c$  denotes the speed of light,  $\mathbf{B}_0^* = \mathbf{B}_0 + \frac{B v_{\parallel}}{\Omega \alpha} \nabla \times \mathbf{b}_0$ ,  $B_0^* = \mathbf{b}_0 \cdot \mathbf{B}_0^*$ .

In GTC, the perturbative  $\delta f$  method is used in the simulation of neoclassical transport [40] to reduce the particle noise. The total distribution function could be separated into equilibrium and perturbation part:  $f_e = f_{0e} + \delta f_e$ . We also expand the  $L$  into two parts, that is  $L = L_0 + \delta L$ , and

$$L_0 = (v_{\parallel} \mathbf{b}_0 + \mathbf{v}_E) \cdot \left( \frac{\partial}{\partial \mathbf{x}} \right)_{E,\mu} + e(v_{\parallel} \mathbf{b}_0 + \mathbf{v}_d) \cdot \nabla \phi \left( \frac{\partial}{\partial E} \right)_{\mathbf{x},\mu} - C(f_{0e}),$$

$$\delta L = \frac{\partial}{\partial t} + v_{\parallel} \frac{\delta \mathbf{B}}{B_0} \cdot \left[ \left( \frac{\partial}{\partial \mathbf{x}} \right)_{E,\mu} - q_s \nabla \phi \left( \frac{\partial}{\partial E} \right)_{\mathbf{x},\mu} \right] + \mathbf{v}_d \cdot \left( \frac{\partial}{\partial \mathbf{x}} \right)_{E,\mu} - C(\delta f_e).$$

Here, we assume that the potential  $\phi(\psi)$  is only the function of flux surface.

The equilibrium distribution function is defined by

$$L_0 f_{0e} = 0. \quad (2)$$

Since the collision operator in  $L_0$  will relax the electron distribution function to the Maxwellian in the ion frame, the solution of  $f_{0e}$  is a shifted Maxwellian

$$f_{0e} = f_{SM} = n_e \left( \frac{m_e}{2\pi T_{0e}} \right)^{\frac{3}{2}} \exp \left( -\frac{2\mu B_0 + m_e(v_{\parallel} - v_{\parallel 0})^2}{2T_{0e}} \right),$$

where  $n_e(\psi, \theta) = n_{0e}(\psi) \exp \left( \frac{m_e v_{\parallel 0}^2}{2T_{0e}} \right)$  and  $T_{0e}(\psi)$  are the equilibrium density and temperature profiles. The  $v_{\parallel 0}$  is the equilibrium ion toroidal rotation, which is determined by the ion radial force balance  $v_{\parallel 0} = \frac{g}{B_0} \Omega_t = -\frac{cg}{B_0} \left( \frac{\partial \phi}{\partial \psi} \right)$ , where the ion pressure gradient is neglected,  $g = RB_{\zeta}$ ,  $R$  is the major radius,  $B_{\zeta}$  is the toroidal component of the magnetic field  $\mathbf{B}_0$ ,  $\Omega_t$  is the angular velocity of the ion toroidal rotation. For single-species simulations of the electrons, the density  $n_e$  is assumed to be a function of flux surface only, since  $v_{\parallel 0} \ll v_{\parallel e}$ .

The perturbed distribution function obeys the following perturbed drift kinetic equation

$$L(\delta f_e) = -\delta L f_{0e} = \mathbf{v}_d \cdot \boldsymbol{\kappa} f_{SM} + v_{\parallel} \frac{\delta \mathbf{B}}{B_0} \cdot \left( \boldsymbol{\kappa} + \frac{e}{T_{0e}} \nabla \phi \right) f_{SM}. \quad (3)$$

Here, higher order terms in  $v_{\parallel 0}/v_{\parallel e}$  are neglected and the equilibrium gradient parameter is defined as

$$\boldsymbol{\kappa} \equiv \left( \kappa_n + \left( \frac{2\mu B_0 + m(v_{\parallel} - v_{\parallel 0})^2}{2T_{0e}} - \frac{3}{2} \right) \kappa_t + \frac{m(v_{\parallel} - v_{\parallel 0})v_{\parallel 0}}{T_{0e}} \kappa_v \right) \nabla \psi,$$

where  $\kappa_n \nabla \psi = -\frac{\nabla n_{0e}}{n_{0e}}$ ,  $\kappa_t \nabla \psi = -\frac{\nabla T_{0e}}{T_{0e}}$ ,  $\kappa_v \nabla \psi = -\frac{g \nabla \Omega_t}{B_0 v_{\parallel 0}}$ .

### 2.3 Verification of GTC simulation of neoclassical transport

In this subsection, we verify simulation results of neoclassical transport for both an axisymmetric circular cross section tokamak and the DIII-D tokamak. In the neoclassical simulation, uniform Maxwellian distribution of electron markers are loaded over an annulus of a tokamak. Based on convergent studies, a total of  $4.23 \times 10^7$  particles are used in all the neoclassical simulations in this paper. Ions are treated as the cold, fixed background.

For the circular cross section tokamak, we use the representative parameters with a major radius  $R_0 = 1.86$  m, a minor radius  $a = 0.246R_0$ , the magnetic field strength on axis  $B_0 = 1.35$  T, uniform electron temperature profile with  $T_e = 5.0$  keV, electric field  $E_r = 0$ , a safety factor profile  $q = 1.475 + 1.1 \frac{\psi}{\psi_w} + 1.0 \frac{\psi^2}{\psi_w^2}$ , a density profile  $n_e = n_0 \left[ 1.0 + 0.205 \left( \tanh \left( 0.75 - 2.5 \frac{\psi}{\psi_w} \right) - 1.0 \right) \right]$ . At  $r = 0.5a$ ,  $q = 2$ ,  $Z_{eff} = 1$ , and  $R_0/L_n = 2.2$  ( $L_n$  is the radial density gradient scale length). The effective electron collision frequency  $\nu^* = \varepsilon^{-3/2} \nu q R_0 / v_{th}$  is defined as the physical collision frequency  $\nu$  normalized by the bounce frequency, where  $\varepsilon = r/R_0$  is the local inverse aspect ratio,  $v_{th} = \sqrt{T_{0e}/m_e}$  is the electron thermal velocity.

For the DIII-D tokamak, figure 2 shows the equilibrium cross section and profiles after the ELM suppression. The 2D plot of the simulation domain is shown in the fig. 2(a). The equilibrium  $n_e$  and  $T_e$  profiles are plotted in fig. 2(b),  $q$  profile and  $\nu^*$  profiles of electron are shown in fig. 2(c), respectively. At the  $q = 4$  rational surface, the density to temperature gradient ratio is  $\kappa_n/\kappa_t \sim 0.5$ ,  $\nu^* = 0.24$ ,  $Z_{eff} = 3$ , and  $\varepsilon = 0.27$  is evaluated on the outmost midplane. In this verification simulation, the  $\kappa_n$  of electron and  $T_e$  are set to be uniform by using the value at  $q = 4$  rational surface ( $\psi = 0.935\psi_w$ ), which is referred to as the rigid rotation case. Other important parameters are  $E_r = 0$ ,  $R_0 = 1.76$  m, the magnetic field strength on axis  $B_0 = 1.8$  T.

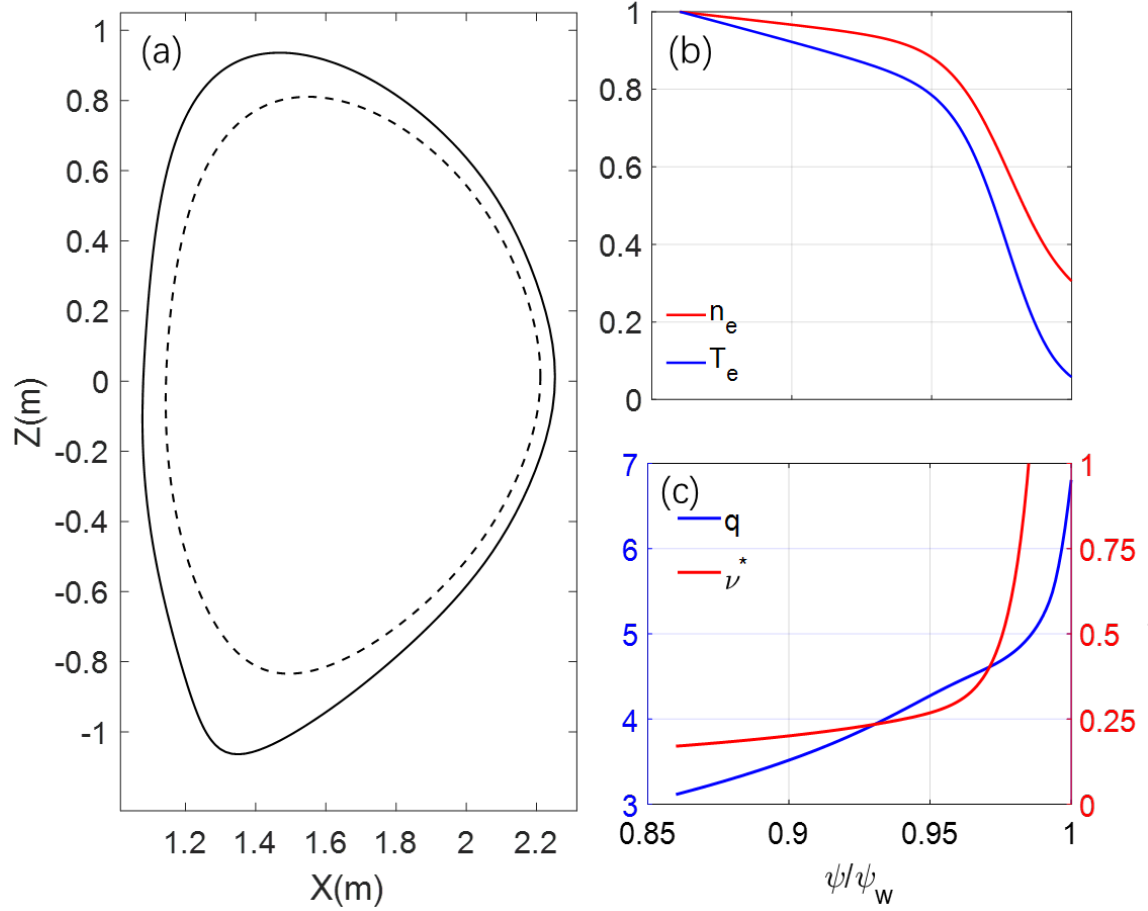


Fig 2. Axisymmetric equilibria of DIII-D discharge #158103 at 3050 ms: (a) Cross section between  $\psi = 0.984\psi_w$  (solid line) and  $\psi = 0.86\psi_w$  (dashed line). (b) Electron density  $n_e$  and temperature  $T_e$  profiles, values on  $\psi = 0.86\psi_w$  are  $2.4 \times 10^{13}\text{cm}^{-3}$  and 1.45 keV. (c) Safety factor  $q$  and electron effective collision frequency  $\nu^*$  profiles.

The neoclassical particle fluxes in the absence of the RMP and electric field are simulated for various collision frequencies to verify the neoclassical simulation model. The relation between electron particle flux  $\Gamma_e$  at steady state versus  $\nu^*$  is plotted in the fig. 3, where  $\Gamma_e = \langle \int \mathbf{v}_d \cdot \nabla \psi \delta f_e d^3 v \rangle$ . For comparison, the analytic values of  $\Gamma_e$  in the banana regime and collisional regime are also plotted. For the circular cross section tokamak, the GTC neoclassical simulation results agree well with the analytic results for [40, 41] in both low and high frequency regimes. For the DIII-D tokamak, the simulation results are slightly smaller than the analytic results in both frequency regimes, presumably due to the shaping and finite aspect ratio effects neglected in the

analytic theory.

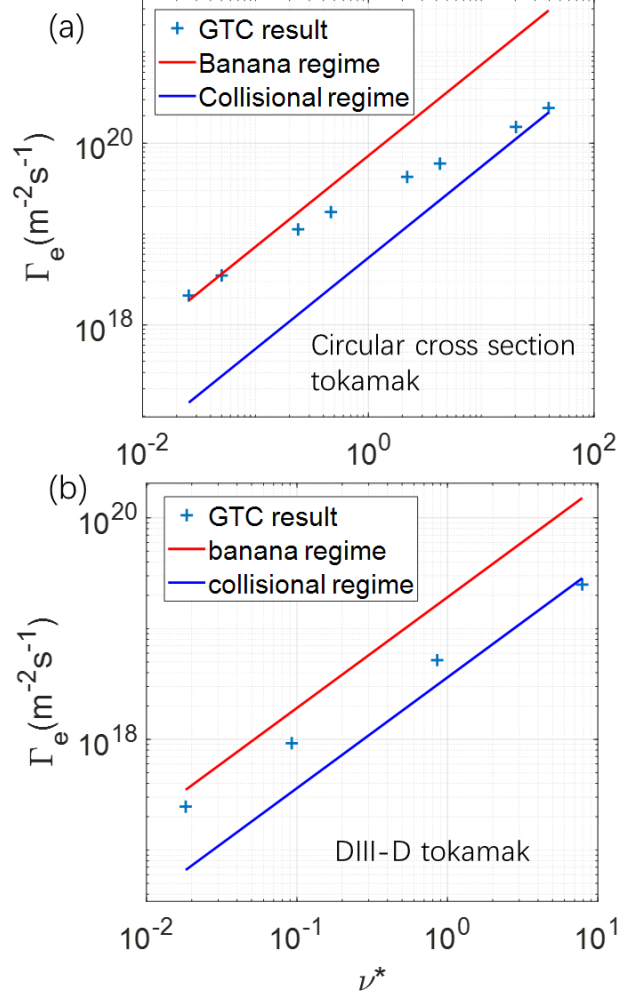


Fig 3. Neoclassical particle flux  $\Gamma_e$  dependence on effective collision frequency  $\nu^*$  without RMP and electric field under circular cross section tokamak (panel a) and DIII-D tokamak (panel b). The solid line is analytic expression in banana regime (red line) and collision regime (blue line).

### 3. Effects of RMP on neoclassical particle flux without equilibrium electric field

We now study effects of the RMP on electron particle fluxes  $\Gamma_e$  using the equilibrium and plasma parameters of the DIII-D discharge #158103 as described in section 2. For simplicity, only the electrons are simulated, assuming that effects of the RMP on the ion transport is much smaller than the electron transport.

#### 3.1 Verification of RMP effects with rigid rotation case

In this subsection, we use the rigid rotation case to verify the effects of the RMP on neoclassical

transport, where the particle fluxes in the presence of the RMP are measured by  $\Gamma_e = \left\langle \int \left( \mathbf{v}_d + v_{\parallel} \frac{\delta \mathbf{B}}{B_0} \right) \cdot \nabla \psi \delta f_e d^3 v \right\rangle$ . Define the non-ambipolar particle flux induced by the RMP  $\Delta \Gamma_e \equiv \Gamma_{RMP} - \Gamma_0$ , where  $\Gamma_{RMP}$  and  $\Gamma_0$  are the neoclassical electron particle fluxes with and without the RMP. Theoretically,  $\Gamma_0$  is intrinsically ambipolar in the limit of small orbit width [38, 40]. However,  $\Gamma_{RMP}$  is not ambipolar and  $\Delta \Gamma_e$  can induce an ambipolar electric field to restore the ambipolarity, similar to the neoclassical transport in stellarators [31].

Fig 4(a) shows the time history of volume-averaged electron particle fluxes  $\Gamma_e$  around 8/2 and 7/2 island regions. The electron particle fluxes reach a steady state after a few collision times  $\tau_e = 1/\nu$ . In the simulation without the RMP, there is no obvious difference between the  $\Gamma_e$  in these two regions. However, in the simulation with the RMP, compared with the 7/2 island, the wider 8/2 island induces a much larger increase of electron particle flux  $\Delta \Gamma_e$  at steady state  $t = 40 \tau_e$ . The  $\Delta \Gamma_e$  induced by the 8/2 island is comparable to the  $\Gamma_0$ , but is much smaller than the turbulent transport level and therefore does not contribute to the density pump out. However, the non-ambipolar particle fluxes can induce an ambipolar electric field, which will be calculated in the section 5.

Fig 4(b) shows the  $\Gamma_e$  radial profiles averaged over  $t = [40, 80] \tau_e$  in the simulations with and without the RMP. Three regions, the 7/2 island region ( $q = 3.44 \sim 3.55$ ), the 8/2 island region ( $q = 3.84 \sim 4.15$ ), and the non-resonant region ( $q = 3.55 \sim 3.84$ ), are separated by the island separatrices. The larger 8/2 island induces a much larger  $\Delta \Gamma_e$  than that in the 7/2 island region and in the non-resonant region, which suggests that the non-ambipolar electron particle flux is mostly driven by the resonant component of the RMP.

Fig 4(c) shows the  $\Delta \Gamma_e$  in the simulations varying the collision frequency  $\nu^* = [0, 0.5]$  in the two island regions. The  $\Delta \Gamma_e$  in the collisionless case is much smaller than that in the simulations with collisions, which indicates that the flutter transport due to magnetic stochasticity is not dominant [42]. The  $\Delta \Gamma_e$  in both the 7/2 and 8/2 island regions slightly decreases with the collision frequency in the banana regime.

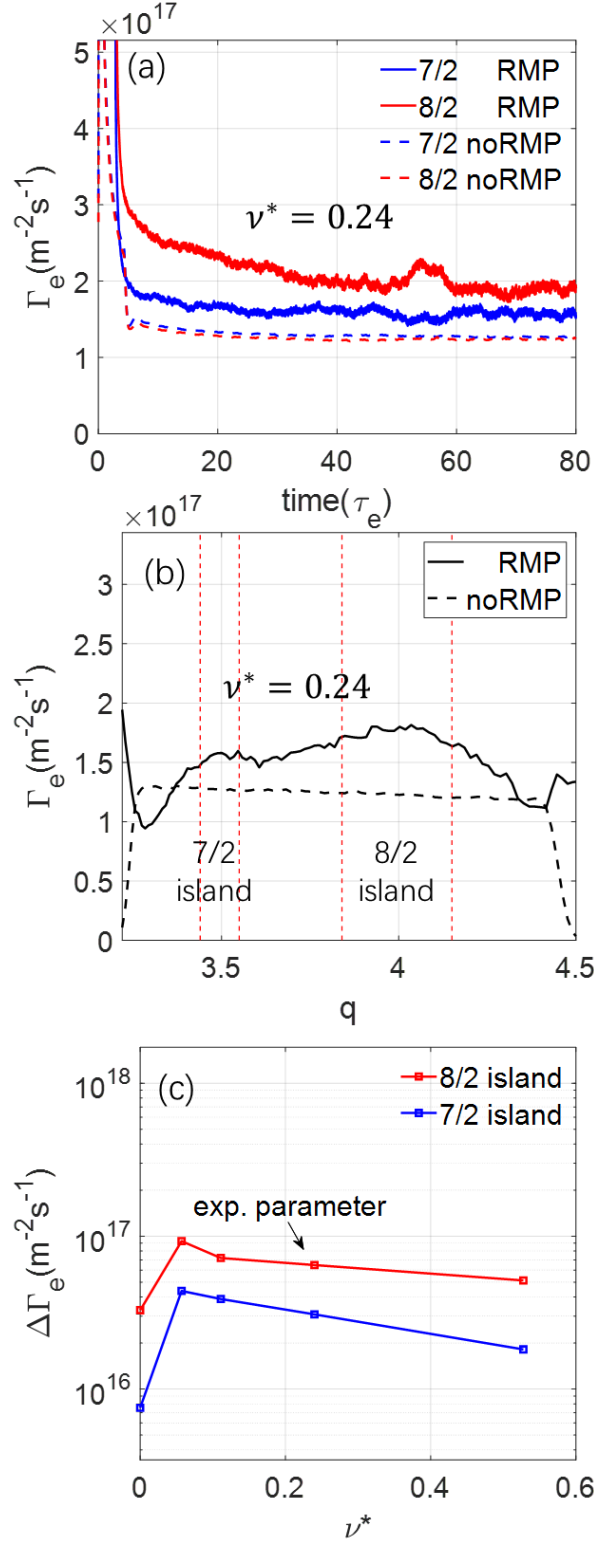


Fig 4. Neoclassical electron particle flux in rigid rotation case. (a) Time history of  $\Gamma_e$  at 7/2 and 8/2 island region in simulations with and without RMP. (b)  $\Gamma_e$  profile averaged over  $t = [40,80] \tau_e$  in simulations with and without RMP. Vertical dashed lines represent island separatrices. (c) Dependence of  $\Delta\Gamma_e$  on collision frequency  $\nu^*$  at 7/2 and 8/2 island region.

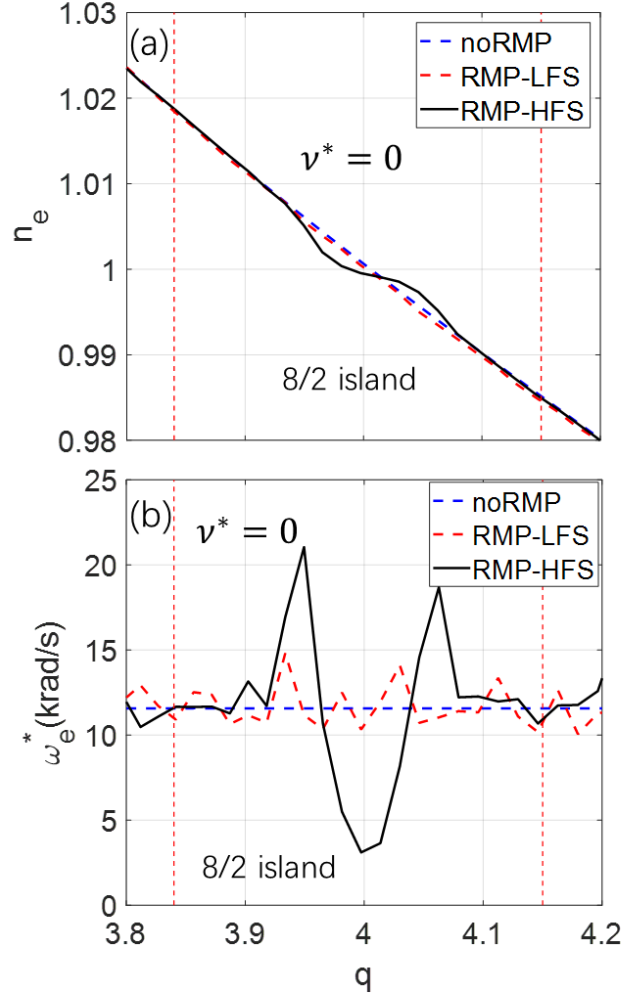


Fig 5. Electron density profiles  $n_e$  (panel a) and diamagnetic frequency  $\omega_e^*$  profiles (panel b) in rigid rotation case in 8/2 island region in collisionless simulations after profile relaxation. Red-dashed and black line are density profiles on low field side and high field side with RMP. Blue-dashed line is density profile without RMP. Vertical dashed lines represent island separatrices.

Fig 5(a) shows the relaxation of electron density profiles in the 8/2 island region in the collisionless simulations with and without the RMP. On the high field side, the electron density profile is locally flattened inside the 8/2 island region and reach the steady state after some bounce times. On the low field side, the electron density profile is less affected by the RMP, because the trapped particles on the low field side do not follow the field line around the magnetic island. In the collisional simulations, the collisions could further modify the density profiles [33].

Fig 5(b) shows the relaxation of electron diamagnetic frequency  $\omega_e^* = -\frac{1}{qn_e e} \frac{\partial n_e T_e}{\partial \psi}$  profiles in the 8/2 island region in the collisionless simulations with and without the RMP. On the low field side, the electron diamagnetic frequency is only slightly affected by the RMP, which is consistent

with the change of density profile on the low field side. On the high field side, the electron diamagnetic frequency is significantly changed across the 8/2 island region, because the density profile is flattened locally.

### 3.2 Simulation with the experimental equilibrium profiles

We now use experimental  $n_e$  and  $T_e$  profiles described in sec. 2.3. Two sets of simulations are carried out with or without the RMP. The first set uses the experimental  $n_e$  profile and a uniform  $T_e = T_e(q = 4)$ , thus  $\kappa_t = 0$ . The second set uses both the experimental  $n_e$  and  $T_e$  profiles as the equilibrium profiles.

Fig 6 shows the steady state  $\Gamma_e$  profiles in the simulations. In the simulations without the RMP, the ambipolar  $\Gamma_e$  in the case with experimental  $T_e$  ( $\kappa_t > 0$ ) is slightly smaller than that in the uniform  $T_e$  ( $\kappa_t = 0$ ) case, which qualitatively agrees with the standard neoclassical theory [41]. In the simulations with the RMP, both uniform  $T_e$  and experimental  $T_e$  profiles can induce the non-ambipolar particle fluxes  $\Delta\Gamma_e$ . We rewrite the non-ambipolar particle flux  $\Delta\Gamma_e = D_0(\kappa_n + \beta\kappa_t)$ , where  $D_0$  is the transport coefficient in the uniform  $T_e$  ( $\kappa_t = 0$ ) case,  $\beta$  denotes the ratio between the contribution from temperature and density gradients. We find that  $\beta = 0.56$ , which is qualitatively consistent with the NTV theory [13].

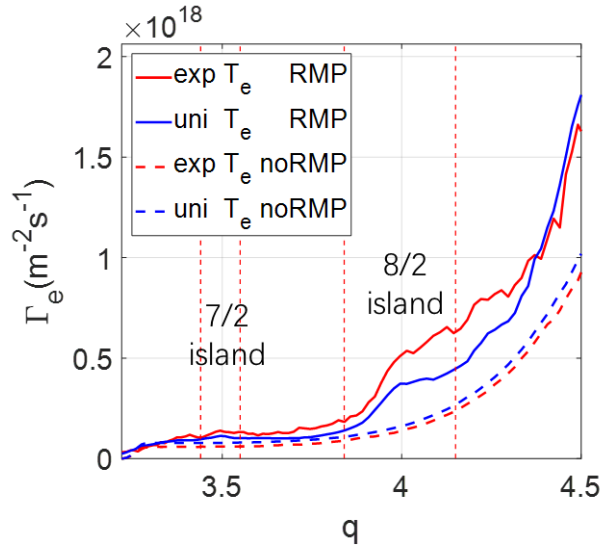


Fig 6. Electron particle flux  $\Gamma_e$  profiles from neoclassical simulations using experimental density profile, experimental  $T_e$  (red line) or uniform  $T_e$  profiles (blue line), with (solid line) and without (dashed line) RMP. Vertical dashed lines represent island separatrices.

The neoclassical simulations use the RMP equilibrium calculated by the M3D-C1, which could have a large uncertainty in the magnetic island width. Therefore, we perform a sensitivity study for the RMP amplitude  $\alpha$ . Fig 7 shows the dependence of  $\Delta\Gamma_e$  on the  $\alpha$  on the  $q=4$  surface from GTC neoclassical simulations using experimental equilibrium profiles, where  $\alpha_0$  is the original RMP amplitude calculated by the M3D-C1. It is clear that  $\Delta\Gamma_e$  follows a quadratic relation with  $\alpha$ , i.e., the non-ambipolar flux is proportional to the magnetic island width.

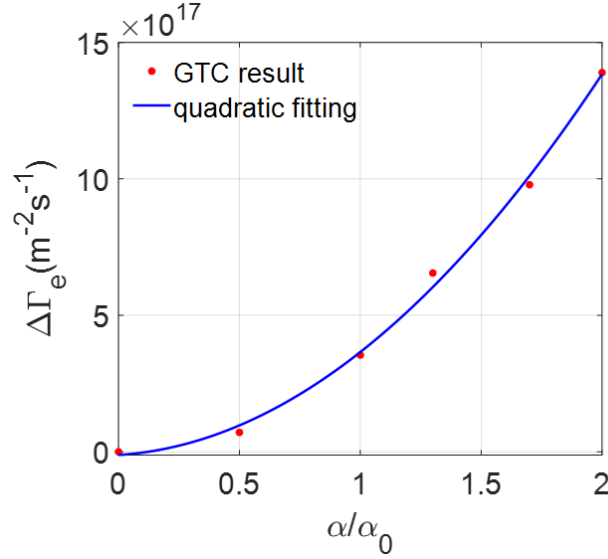


Fig 7. Dependence of non-ambipolar electron particle flux  $\Delta\Gamma_e(q = 4)$  on RMP amplitude  $\alpha$  from neoclassical simulation. The blue line is a quadratic fit.

#### 4. Effect of RMP on neoclassical particle flux with equilibrium electric field

In this section, the effects of equilibrium electric field  $E_r$  on the neoclassical transport is studied. During the time scale of the ELM suppression ( $\sim 1$  ms), the equilibrium density and temperature profiles do not change much, but the equilibrium electric field  $E_r$  can change significantly, which can affect the neoclassical and turbulent transport [11, 29].

Fig 8(a) shows the radial profiles of the experimental equilibrium  $E_r$  on the outer midplane during the ELMing (3796ms) and ELM suppression (3050ms) in the DIII-D discharge #158103. In this section, these two  $E_r$  profiles, together with the  $n_e$  and  $T_e$  profiles at 3050 ms, are used as the equilibrium.

First, we verify the effects of the equilibrium electric field  $E_r$  using the uniform  $\kappa_n$  and  $T_e$

profiles with the value at the  $q = 4$  flux surface. Uniform  $E_\psi = -\frac{\partial\phi}{\partial\psi}$  profiles (rigid rotation case) or experimental  $E_r$  profiles are used in the simulations separately. Fig 8(b) shows the  $\Delta\Gamma_e$  near the  $q = 4$  surface at the steady state of neoclassical simulations using the equilibrium with the RMP and the uniform electric field  $E_\psi$ . Here, we use  $E_N \equiv -\frac{\partial\phi}{\partial\psi}/\frac{T_\alpha}{q_\alpha}\kappa_n$  to represent the amplitude of the electric field, which corresponds to the ratio between the  $\mathbf{E} \times \mathbf{B}$  and diamagnetic flows. The  $E_N$  values of 2.9 and -0.22 correspond to the local value of the electric field during the ELMing and the ELM suppression, respectively. The value of  $E_N = -1$  corresponds to the toroidal rotation frequency  $\Omega_{te} = 0$ . In the rigid rotation case, when  $E_N = -1$ , the  $\Delta\Gamma_e$  is three orders of magnitude smaller than the neoclassical particle flux without the effect of RMP. When the  $E_N \neq -1$ , the absolute value of the  $\Delta\Gamma_e$  begins to increase, which can change the radial electric field and damp the rotation, in qualitative agreement with the neoclassical theory [41, 43] predicting the toroidal flow damping by the toroidal viscosity due to the 3D magnetic fields.

In the simulations using the experimental  $E_r$  profiles without the RMP, the shear of the equilibrium electric field  $E_r$  has little effects on the  $\Gamma_e$ , because the electrons banana orbit width is much smaller than the radial scale length of the electric field. In the simulations with the RMP, both the experimental  $E_r$  profiles during the ELMing and the ELM suppression are found to induce additional positive  $\Delta\Gamma_e$  when compared with the uniform electric field. The value of  $\Delta\Gamma_e$  in the simulation with the  $E_r$  during the ELMing is much larger than that during the ELM suppression, which indicates that the rotation damping during the ELMing is much larger than that during the ELM suppression.

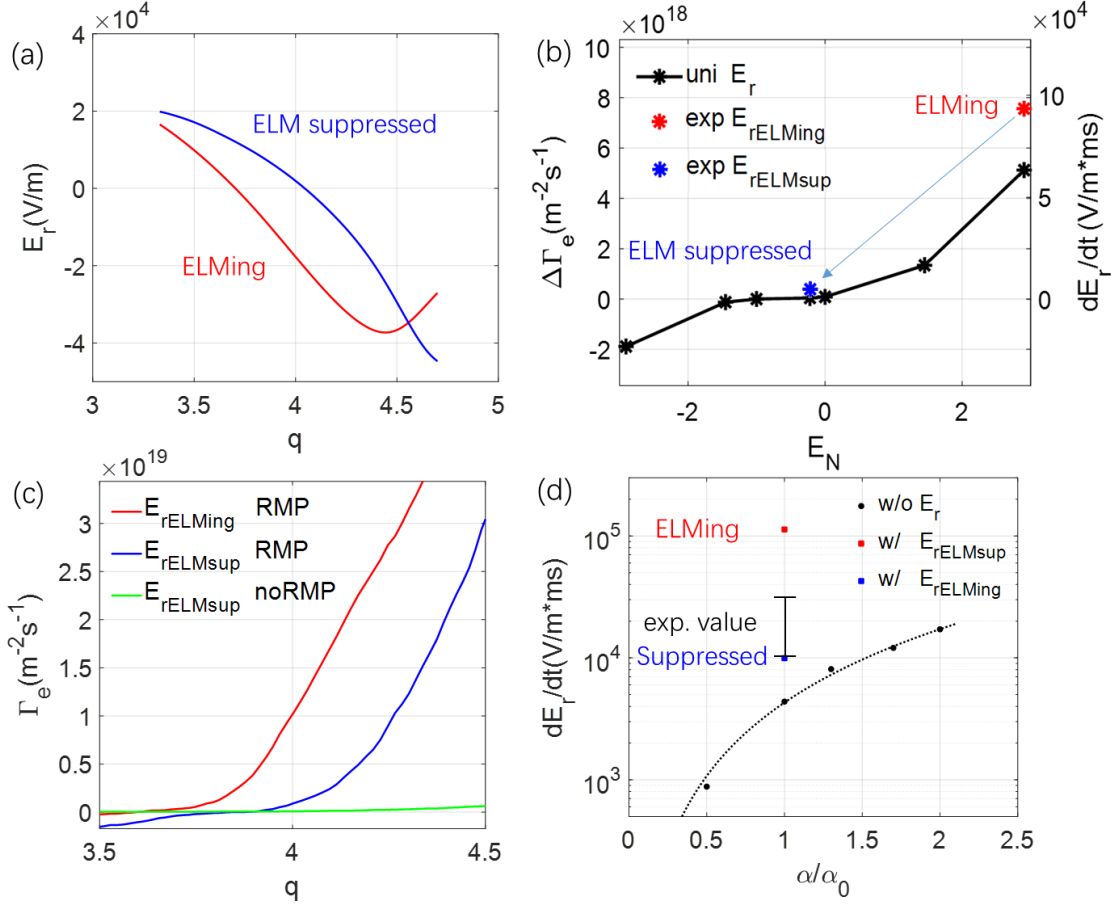


Fig 8. (a) Equilibrium electric field  $E_r$  profiles of DIII-D for 158103 discharge during ELMing and ELM suppression. (b) Dependence of non-ambipolar particle flux  $\Delta\Gamma_e$  on electric field amplitude  $E_N$  in simulations with uniform and experimental  $E_r$  profiles, using the uniform  $\kappa_n$  and  $T_e$  profiles. (c) Profiles of  $\Gamma_e$  at steady state of neoclassical simulations with  $E_r$  profiles during ELMing (blue line) and ELM suppression (red line), and without RMP (yellow line), using experimental density and temperature profiles. (d) Dependence of time rate of change of  $E_r$  on RMP amplitude  $\alpha$  from simulations without equilibrium  $E_r$  and with equilibrium  $E_r$  during ELMing and ELM suppression. Error bar represents experimental value with 50% uncertainty range.

Finally, to compare with the experimental measurements of rotation damping, we carry out simulations using the experimental  $n_e$ ,  $T_e$ , and the two  $E_r$  profiles. Fig 8 (c) shows the  $\Gamma_e$  profiles at the steady state of these neoclassical simulations with or without the RMP. In the simulations without the RMP, the shear of  $E_r$  has little effects on the  $\Gamma_e$ , same as the simulation results in the rigid rotation case. In the simulations with the RMP, the  $E_r$  profile during the ELMing induces a much larger non-ambipolar particle flux  $\Delta\Gamma_e$  than that during the ELM suppression. This indicates that the non-ambipolar particle flux  $\Delta\Gamma_e$  can drop drastically during the ELM suppression, which is mainly due to the rapid change of the equilibrium electric field  $E_r$ . The sensitivity of the

electron flux on the equilibrium electric field indicates that some electron orbits become stochastic due to the RMP.

## 5. Rotation damping rate due to non-ambipolar particle flux

In this section, we calculate the damping rate of the toroidal rotation by calculating the time rate of change of the electric field  $E_r$  using the non-ambipolar particle flux  $\Delta\Gamma_e$  measured in the steady state of the neoclassical simulations in the previous sections. Combining the gyrokinetic Poisson's equation and guiding center continuity equation, the quasi-neutrality condition takes the form [44],

$$\frac{dE_\psi}{dt} \left\langle \frac{|\nabla\psi|^2}{B^2} \right\rangle = -\frac{1}{m_i n_i c^2} \sum_s q_s \left\langle \int d^3v f_s \left( \mathbf{v}_d + \mathbf{v}_E + v_\parallel \frac{\delta\mathbf{B}}{B_0} \right) \cdot \nabla\psi \right\rangle. \quad (4)$$

Here, the subscript  $s$  denotes the particle species (i for ion and e for electron). The flux-surface-averaged polarization current on the left hand side cancels out with the guiding center current on the right hand side. The relation between  $E_\psi \equiv -\frac{\partial\phi}{\partial\psi}$  and radial electric field  $E_r$  is  $E_r = E_\psi |\nabla\psi|$ . The  $\Gamma_i$  and  $\Gamma_e$  are assumed to be ambipolar without the effects of RMP. For the non-ambipolar particle fluxes, only the electron contribution is taken into account by assuming that the ion contribution is negligible. Equation (4) is then used to calculate the damping rate of the toroidal rotation.

Fig. 7(d) shows the damping rate calculated from the simulations using the experimental  $n_e$ ,  $T_e$  and the two experimental  $E_r$  profiles plotted in Fig. 7(a). When comparing simulation results with the experimental measurement of the damping rate during the ELM suppression, two aspects of uncertainty should be considered. The first one comes from the MHD simulations of the RMP amplitude  $\alpha$ . In the  $\alpha$  amplitude scanning, the damping rate is about one third of the experimental level when  $\alpha = \alpha_0$ , but reaches the experimental level when using  $\alpha = 2\alpha_0$ . The second uncertainty comes from the rapid change of the  $E_r$  during the transition from ELMing to ELM suppression. The damping rate is proportional to the non-ambipolar particle fluxes  $\Delta\Gamma_e$ , which depends on the  $E_r$  amplitude and shear. From the ELMing and ELM suppression state, the damping rate decreases drastically due to the change of the equilibrium electric fields. This result is consistent with the experiment, in which the toroidal rotation experiences a large torque before the onset of the ELM suppression, followed by relatively small torque after the transition to the ELM

suppression state. The simulated damping rate during the ELM suppression qualitatively agrees with the experimental value.

## 6. Effects of RMP on collisionless damping of zonal flows

To understand the RMP effects on zonal flow dynamics, collisionless zonal flow damping and geodesic acoustic mode (GAM) are simulated by using two types of the 3D RMP fields. Besides the RMP equilibrium described above, another equilibrium is obtained from the ideal MHD code VMEC [45][27], which includes only the non-resonant response of the RMP and thus preserves the closed flux surfaces. For the VMEC equilibrium, an electrostatic version of the fluid-kinetic hybrid electron model [46] is used to treat the kinetic electrons. In this model, the perturbed electron distribution function is represented by  $\delta f_e = \delta f_e^{(0)} + \delta h_e$ , where  $\delta f_e^{(0)}$  is the adiabatic response to the non-zonal electric field, and  $\delta h_e$  is the nonadiabatic response. For the M3D-C1 equilibrium with magnetic islands, the drift kinetic equation DKE [34] is used for solving the electron perturbed distribution function. Both the zonal and nonzonal electric field components are solved together in the presence of magnetic islands. The ion dynamics is simulated by solving the standard gyrokinetic equation. The radial particle flux in this section is defined as

$$\Gamma_e = \left\langle \int d^3v \delta h_e (\mathbf{v}_d + \mathbf{v}_E) \cdot \nabla \psi \right\rangle$$

for the electrons in the hybrid model using the VMEC equilibrium, and

$$\Gamma_s = \left\langle \int d^3v \delta f_e \left( \mathbf{v}_d + \mathbf{v}_E + v_{\parallel} \frac{\delta \mathbf{B}}{B_0} \right) \cdot \nabla \psi \right\rangle, (s = i, e)$$

for the ions and the electrons in the DKE model using the M3D-C1 equilibrium. Here the term  $\delta f_e^{(0)}$  is not included in the  $\Gamma_e$  diagnostic in the hybrid model, which does not affect the self-consistent simulations.

In these simulations, a flux-surface-averaged ion guiding center density perturbation is initiated to generate the zonal flows. The radial profile of the zonal flows is set to be a sin-function with a radial wavevector  $k_r \rho_i = 0.4$ . The density perturbation is set to be zero at the inner and outer boundaries of the simulation domain  $\psi = [0.90, 0.97] \psi_w$ . Simulations in this section use uniform equilibrium density and temperature profiles for both ions and electrons ( $T_i \approx 1.7T_e$ ), corresponding to the local parameters at the  $q = 4$  surface of the DIII-D experiment.

Fig 9(a) shows the time evolution of the radial electric field  $E_r$  of the zonal flows on the  $q=4$

surface in the simulation using adiabatic electrons and the VMEC equilibrium without RMP, with RMP and with RMP\*10 (by artificially amplifying ten times the RMP field amplitude). We can see that the radial electric field evolves with a finite frequency, i.e., damped GAM oscillation, and then reaches a steady state. In the simulation with the RMP, the residual flow is only slightly affected. However, the simulation with the RMP\*10 has a 27% reduction of the residual level after  $t = 50 R_0/c_s$ . Here, the  $R_0$  is the major radius at magnetic axis,  $c_s = \sqrt{T_e/m_i}$  is the speed of ion acoustic wave. The zonal flow residual level is much higher than the Rosenbluth-Hinton theory [47], which neglects shaping effect and finite aspect ratio.

Next, we study effects of kinetic electrons by using gyrokinetic ions and fluid-kinetic hybrid electron model [46]. The time evolution of the radial electric field  $E_r$  of the zonal flows using the VMEC equilibrium with various RMP amplitudes (without RMP, or amplified by 1, 2, 5, 10 times) are shown in the fig 9(b). In the simulation without the RMP, the zonal flow residual level is very close to that in the simulation with the adiabatic electrons, which indicates that the effect of the kinetic electrons in zonal flow damping could be neglected without the RMP. In the simulations with different RMP amplitudes, the change of the residual flow  $\Delta E_r$  is defined as the difference between the  $E_r$  and that in the simulation without the RMP at the same simulation time. The  $\Delta E_r$  is found to depend quadratically on the RMP amplitude, which is consistent with that in the section 3.3. As shown in the fig 9(c), the change of the residual flow  $\Delta E_r$  at  $t = 50 R_0/c_s$  could reach 60%, when the RMP amplitude is amplified by 10 times.

Fig 9(d) shows the time history of radial particle fluxes for the ion  $\Gamma_i$  and electron  $\Gamma_e$  in simulations without RMP and RMP\*10. The  $\Gamma_i$  oscillates with the GAM frequency before  $t = 10 R_0/c_s$ . Subsequently, the  $\Gamma_i$  gradually drops to a much lower level in both the simulations. On the other hand, the  $\Gamma_e$  stays at a high level before  $t = 40 R_0/c_s$  in the simulation with RMP\*10, but is always very small in the simulation without the RMP. This indicates that electron orbits could become stochastic due to the large RMP amplitude, and the residual flow damping is mainly induced by electrons, rather than ions. This result may have implications on zonal flow dynamics in the tokamaks with ripple fields and in the stellarators.

Finally, to study the effects of the RMP islands on zonal flow damping, the M3D-C1 equilibrium is used. The time evolution of the radial electric field  $E_r$  of the zonal flows with

various RMP amplitudes (without RMP, with RMP and RMP\*2) are shown in the fig 10(a). In the simulation without the RMP, the residual zonal flow is close to the result of the VMEC equilibrium within a difference of 20%, which could be due to the differences in the equilibrium and simulation model. The GAM oscillation (during  $0 \sim 5 R_0/c_s$ ) is strongly damped when the RMP amplitude increases. The residual flow in the simulation with the RMP\*2 amplitude with the magnetic islands has a 30% reduction, which is much larger than that in the simulation using the VMEC equilibrium without magnetic islands.

Fig 10(b) shows the ion and electron particle fluxes in simulations without RMP and with RMP\*2 using the M3D-C1 equilibrium with magnetic islands. In the simulation without the RMP, the electron particle flux  $\Gamma_e$  oscillation is strong during the GAM oscillation, which is mainly due to the non-zonal electric fields ( $m \neq 0, n = 0$ ). This electron flux is not visible in Fig. 8d, where we do not include the adiabatic response  $\delta f_e^{(0)}$  in the diagnostic of  $\Gamma_e$ . However, this electron flux does exist in the simulations using the hybrid model through the product of  $\delta f_e^{(0)}$  with  $\mathbf{v}_d$ . In the simulation with RMP\*2, the electron particle flux  $\Gamma_e$  changes strongly at the early time ( $< 2 R_0/c_s$ ), which is mainly due to the magnetic flutter effect from the fast parallel motion of the electrons. The GAM oscillation is then strongly damped by this radial transport.

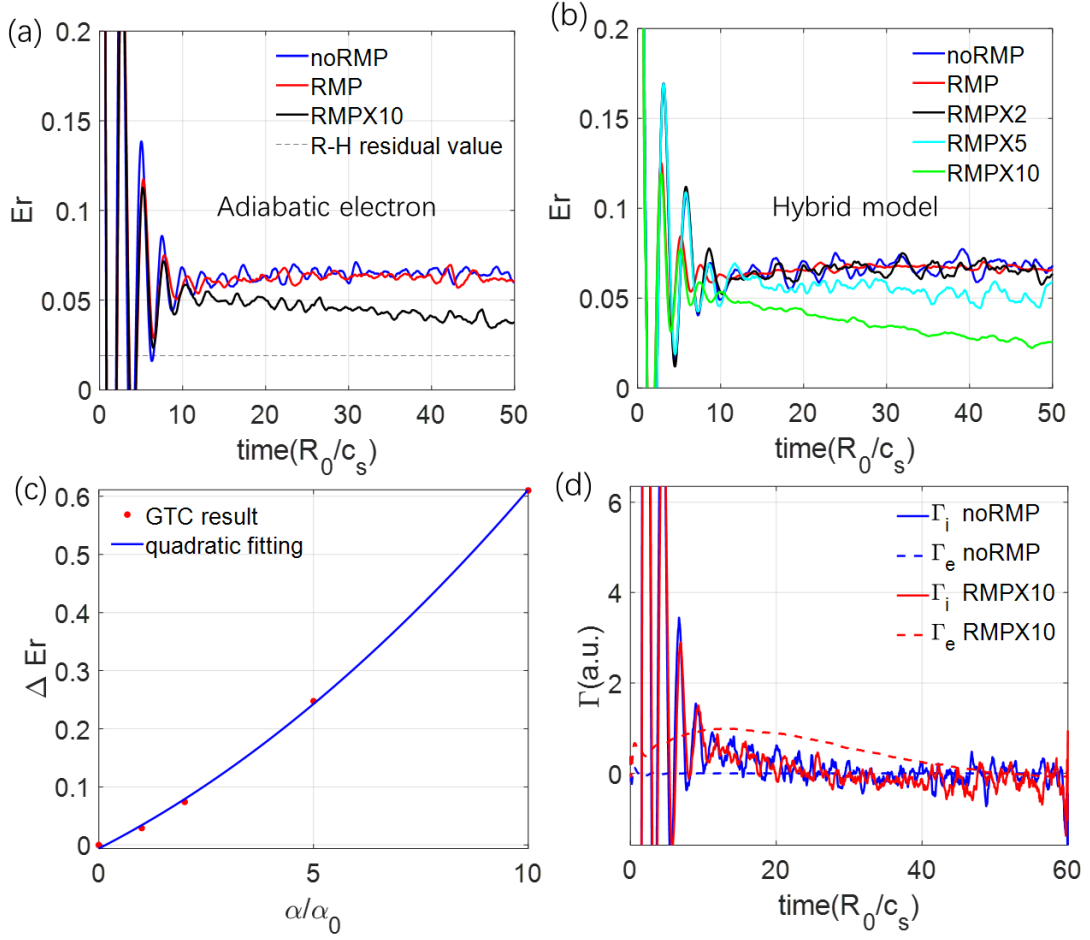


Fig 9. In simulations using VMEC equilibrium with closed flux surfaces, time evolution of radial electric field  $E_r$  of zonal flow with adiabatic electrons (panel a) and kinetic electrons (panel b) with various RMP amplitudes, (c) relation between change of the residual flow  $\Delta E_r$  at  $t = 50 R_0/c_s$  and RMP amplitude  $\alpha$ , (d) radial particle flux (arbitrary unit) of ion  $\Gamma_i$  (solid lines) and electron  $\Gamma_e$  (dashed lines) during zonal flow damping process without RMP (blue lines) and with RMP\*10 (red lines).  $E_r$  is normalized with initial value,  $\Delta E_r$  is normalized with residual flow without RMP, and particle flux is normalized with maximal value of  $\Gamma_e$  in simulation with RMP\*10.

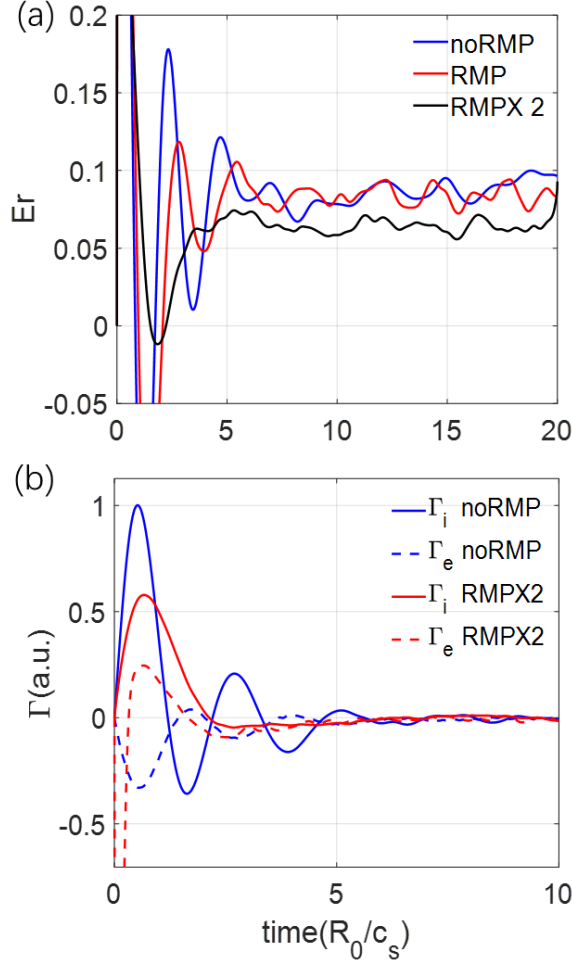


Fig 10. Time evolution of radial electric field  $E_r$  of zonal flows (panel a), ion and electron radial particle fluxes (panel b), with various RMP amplitudes in simulations using M3D-C1 equilibrium including magnetic islands.  $E_r$  is normalized with initial value, particle fluxes are normalized with maximal value of ion particle flux  $\Gamma_i$  in simulation without RMP.

## 7. Conclusion and discussion

In this paper, we use GTC simulations to study the RMP effects on radial electric fields, including both equilibrium electric fields associated with toroidal rotation and zonal flows. The GTC simulations use realistic DIII-D tokamak equilibrium with both resonant and non-resonant responses to 3D RMP calculated by resistive MHD code M3D-C1. Neoclassical simulations show that the 3D RMP-induced magnetic islands and stochastic electron orbits can drive non-ambipolar electron particle fluxes, which lead to a rapid change of equilibrium radial electric field, consistent with the experimental observations during the transition from ELMing to ELM suppression state. The GTC neoclassical simulation results provide a support for the conjecture that the RMP-induced

change of radial electric fields lead to enhanced turbulent transport at the pedestal top during ELM suppression. Furthermore, GTC simulations of collisionless damping of zonal flows find that resonant response to the RMP can decrease the residual level and damp the GAM.

In future simulations, we will couple tokamak core with scrape-off layer (SOL) including magnetic separatrix, which could incorporate ion orbit loss near the separatrix. We will also develop the coupled neoclassical and turbulence simulations. Furthermore, the RMP-induced energetic particles transport will also be studied by GTC.

### **Acknowledgements**

The authors would like to thank J. Bao, L. Shi and S. Taimourzadeh for useful discussion, and acknowledge technical support by the GTC team. This work was supported by the China National Magnetic Confinement Fusion Science Program (Grant No. 2017YFE0301300 and 2018YFE0304100); by the U.S. Department of Energy (DOE) SciDAC ISEP Center and by Princeton Plasma Physics Laboratory under Contract DE-AC02-09CH11466. This work used the resources of the Oak Ridge Leadership Computing Facility at the Oak Ridge National Laboratory (DOE Contract No. DE-AC05-00OR22725) and the National Energy Research Scientific Computing Center (DOE Contract No. DE-AC02-05CH11231). The work used data from the DIII-D National Fusion Facility, a DOE Office of Science user facility, under Awards DE-FC02-04ER54698. DIII-D data shown in this paper can be obtained in digital format by following the links at [https://fusion.gat.com/global/D3D\\_DMP](https://fusion.gat.com/global/D3D_DMP).

This report was prepared as an account of work sponsored by an agency of the United States Government. Neither the United States Government nor any agency thereof, nor any of their employees, makes any warranty, express or implied, or assumes any legal liability or responsibility for the accuracy, completeness, or usefulness of any information, apparatus, product, or process disclosed, or represents that its use would not infringe privately owned rights. Reference herein to any specific commercial product, process, or service by trade name, trademark, manufacturer, or otherwise does not necessarily constitute or imply its endorsement, recommendation, or favoring by the United States Government or any agency thereof. The views and opinions of authors expressed herein do not necessarily state or reflect those of the United States Government or any agency thereof.

### **References**

- [1] T E Evans. "Edge localized modes: recent experimental findings and related issues." *Plasma Physics and Controlled Fusion* 49.7 (2007): S43.
- [2] Lang, P. T., et al. "ELM control strategies and tools: status and potential for ITER." *Nuclear Fusion* 53.4 (2013): 043004.
- [3] Evans, Todd E., et al. "Edge stability and transport control with resonant magnetic perturbations in collisionless tokamak plasmas." *nature physics* 2.6 (2006): 419.

- [4] M.R. Wade et al "Advances in the physics understanding of ELM suppression using resonant magnetic perturbations in DIII-D." Nucl. Fusion (2015) 55 023002
- [5] Unterberg, E. A., et al. "The effects of an open and closed divertor on particle exhaust during edge-localized mode suppression by resonant magnetic perturbations in DIII-D." Nuclear Fusion 50.3 (2010): 034011.
- [6] Liang, Y., et al. "Active control of type-I edge-localized modes with  $n=1$  perturbation fields in the JET tokamak." Physical review letters 98.26 (2007): 265004.
- [7] Team, ASDEX Upgrade, et al. "First observation of edge localized modes mitigation with resonant and nonresonant magnetic perturbations in ASDEX Upgrade." Physical Review Letters 106.22 (2011): 225004.
- [8] Jeon, Y. M., et al. "Suppression of edge localized modes in high-confinement KSTAR plasmas by nonaxisymmetric magnetic perturbations." Physical review letters 109.3 (2012): 035004.
- [9] Paz-Soldan, C., et al. "Observation of a multimode plasma response and its relationship to density pumpout and edge-localized mode suppression." Physical review letters 114.10 (2015): 105001.
- [10] Nazikian, Raffi, et al. "Pedestal bifurcation and resonant field penetration at the threshold of edge-localized mode suppression in the DIII-D tokamak." Physical review letters 114.10 (2015): 105002.
- [11] Taimourzadeh, Sam, et al. "Effects of RMP-induced changes of radial electric fields on microturbulence in DIII-D pedestal top." Nuclear Fusion (2019).
- [12] R. Fitzpatrick. "Interaction of tearing modes with external structures in cylindrical geometry (plasma)", 1993 Nucl. Fusion 33 1049.
- [13] Shaing, Ker-Chung, K. Ida, and S. A. Sabbagh. "Neoclassical plasma viscosity and transport processes in non-axisymmetric tori." Nuclear Fusion 55.12 (2015): 125001.
- [14] Zhu, W., et al. "Observation of plasma toroidal-momentum dissipation by neoclassical toroidal viscosity." Physical review letters 96.22 (2006): 225002.
- [15] Sun, Y., et al. "Non-resonant magnetic braking on JET and TEXTOR." Nuclear Fusion 52.8 (2012): 083007.
- [16] Park, J-K., et al. "Rotational resonance of nonaxisymmetric magnetic braking in the KSTAR tokamak." Physical review letters 111.9 (2013): 095002.
- [17] Logan, Nikolas C., et al. "Dependence of neoclassical toroidal viscosity on the poloidal spectrum of applied nonaxisymmetric fields." Nuclear Fusion 56.3 (2016): 036008.
- [18] Li, X. Y., et al. "Rotation braking with  $n=1$  nonaxisymmetric magnetic perturbation in the EAST tokamak." Physics of Plasmas 26.5 (2019): 052512.
- [19] Yueqiang Liu et al. "Role of 3D neoclassical particle flux in density pump-out during ELM control by RMP in DIII-D." Nucl. Fusion 60 (2020) 036018. [20] Park, G., et al. "Plasma transport in stochastic magnetic field caused by vacuum resonant magnetic perturbations at diverted tokamak edge." Physics of Plasmas 17.10 (2010): 102503.
- [21] Kim, Kimin, et al. " $\delta f$  Monte Carlo calculation of neoclassical transport in perturbed tokamaks." Physics of Plasmas 19.8 (2012): 082503.
- [22] Waltz, R. E., and F. L. Waelbroeck. "Gyrokinetic simulations with external resonant magnetic perturbations: Island torque and nonambipolar transport with plasma rotation." Physics of Plasmas 19.3 (2012): 032508.
- [23] Kwon, Jae-Min, et al. "Gyrokinetic simulation study of magnetic island effects on neoclassical

- physics and micro-instabilities in a realistic KSTAR plasma." *Physics of Plasmas* 25.5 (2018): 052506.
- [24] Heyn, M. F. et al. "Quasilinear modelling of RMP interaction with a tokamak plasma: application to ASDEX Upgrade ELM mitigation experiments." *Nucl. Fusion*. 54, 064005 (2014).
- [25] Park, Jong-kyu, et al. "Importance of plasma response to nonaxisymmetric perturbations in tokamaks." *Physics of Plasmas* 16.5 (2009): 056115.
- [26] Z. Lin, T. S. Hahn, W. W. Lee, W. M. Tang, and R. B. White, "Turbulent Transport Reduction by Zonal Flows: Massively Parallel Simulations." *Science* 281, 1835 (1998).
- [27] Holod, Ihor, et al. "Effect of resonant magnetic perturbations on microturbulence in DIII-D pedestal." *Nuclear Fusion* 57.1 (2016): 016005.
- [28] Hager, Robert, et al. "Gyrokinetic study of collisional resonant magnetic perturbation (RMP)-driven plasma density and heat transport in tokamak edge plasma using a magnetohydrodynamic screened RMP field." *Nuclear fusion* 59.12(2019):126009.1-126009.14.
- [29] Hager, Robert, et al. "Gyrokinetic understanding of the edge pedestal transport driven by resonant magnetic perturbations in a realistic divertor geometry." *Phys. Plasmas* 27, 062301 (2020).
- [30] H. Y. Wang, I. Holod, Z. Lin, J. Bao, J. Y. Fu, P. F. Liu, J. H. Nicolau, D. Spong, and Y. Xiao, "Global Gyrokinetic Particle Simulations of Microturbulence in W7-X and LHD Stellarators." *Phys. Plasmas* 27, 082305 (2020).
- [31] J. Y. Fu, J. H. Nicolau, P. F. Liu, X. S. Wei, Y. Xiao, and Z. Lin. "Global gyrokinetic simulation of neoclassical ambipolar electric field and its effects on microturbulence in W7-X stellarator", submitted to *Physics of plasma*.
- [32] P. Jiang, Z. Lin, I. Holod, C. J. Xiao, "The Implementation of Magnetic Islands in Gyrokinetic Toroidal Code", *Plasma Sci. Technol.* 18, 126 (2016)
- [33] Dong, G., and Z. Lin. "Effects of magnetic islands on bootstrap current in toroidal plasmas." *Nuclear Fusion* 57.3 (2016): 036009.
- [34] Fang, K. S., and Z. Lin. "Global gyrokinetic simulation of microturbulence with kinetic electrons in the presence of magnetic island in tokamak." *Physics of Plasmas* 26.5 (2019): 052510.
- [35] Fang K S, Bao J and Lin Z H "Gyrokinetic simulations of nonlinear interactions between magnetic islands and microturbulence." *Plasma Sci. Technol.* 21, 115102, (2019)
- [36] Ferraro, N. M. "Calculations of two-fluid linear response to non-axisymmetric fields in tokamaks." *Physics of Plasmas* 19.5 (2012): 056105.
- [37] Yong Xiao, Ihor Holod, Zhixuan Wang, Zhihong Lin, and Taige Zhang, "Gyrokinetic particle simulation of microturbulence for general magnetic geometry and experimental profiles." *Phys. Plasmas* 22, 022516 (2015).
- [38] Kanno, R, et al. "Development of a Drift-Kinetic Simulation Code for Estimating Collisional Transport Affected by RMP and Radial Electric Field." *Contributions to Plasma Physics* 56, No. 6-8, 592 – 597 (2016).
- [39] White, R. B., and M. S. Chance. "Hamiltonian guiding center drift orbit calculation for plasmas of arbitrary cross section." *The Physics of fluids* 27.10 (1984): 2455-2467.
- [40] Lin, Z., W. M. Tang, and W. W. Lee. "Gyrokinetic particle simulation of neoclassical transport." *Physics of Plasmas* 2.8 (1995): 2975-2988.
- [41] Hinton, F. L., and Richard D. Hazeltine. "Theory of plasma transport in toroidal confinement systems." *Reviews of Modern Physics* 48.2 (1976): 239.
- [42] A. B. Rechester and M. N. Rosenbluth, "Electron Heat Transport in a Tokamak with Destroyed

Magnetic Surfaces." Phys. Rev. Lett. 40, 38, (1979)

[43] Cole, A. J., C. C. Hegna, and J. D. Callen. "Effect of neoclassical toroidal viscosity on error-field penetration thresholds in tokamak plasmas." Physical review letters 99.6 (2007): 065001.

[44] Wang, W. X., F. L. Hinton, and S. K. Wong. "Neoclassical radial electric field and transport with finite orbits." Physical review letters 87.5 (2001): 055002.

[45] S. P. Hirshman, and J. C. Whitson, "Steepest-descent moment method for three-dimensional magnetohydrodynamic equilibria." The Physics of Fluids 26, 3553 (1983)

[46] Z Lin et al "Global gyrokinetic particle simulations with kinetic electrons." Plasma Phys. Control. Fusion 49 B163, (2007)

[47] M. N. Rosenbluth and F. L. Hinton, "Poloidal Flow Driven by Ion-Temperature-Gradient Turbulence in Tokamaks." Phys. Rev. Lett. 80,724, (1998)